Check for updates

Designing high energy density flow batteries by tuning active-material thermodynamics†

Shyam K. Pahari, [a] Tugba Ceren Gokoglan,[b] Benjoe Rey B. Visayas, [a]
Jennifer Woehl,[a] James A. Golen,[a] Rachael Howland,[a] Maricris L. Mayes, [a]
Ertan Agar [b] and Patrick J. Cappillino [*a]

The cost of electricity generated by wind and solar installations has become competitive with that generated by burning fossil fuels. While this paves the way for a carbon-neutral electrical grid, short- and long-term intermittency necessitates energy storage. Flow batteries are a promising technology to accommodate this need, with numerous advantages, including decoupled power and energy ratings, which imparts flexibility, thermal stability, and safety. Further, development of robust nonaqueous systems has the potential to greatly improve energy density, approaching that of lithium-ion batteries, while maintaining the advantages of flow systems. Herein we report a breakthrough on a bio-inspired nonaqueous redox flow battery (NRFB) electrolyte, which contains high-concentration active-material and maintains stability during deep cycling for extended time-periods. These advances are reinforced by thermodynamic considerations and computational investigations, which provide a clear path to further improvements. Electrochemical studies confirm that the active-material maintains its high stability at high concentration. This molecular scaffold clears two important hurdles in designing active-materials for nonaqueous electrolytes – low solubility and poor stability – providing an in-road to development of high-performance NRFB systems.

Introduction

Over the last decade, the cost of renewable energy has decreased markedly. Since 2010, the cost of utility-scale energy from photovoltaics has dropped more than 75% to less than $1/W and the price of wind turbines has fallen 58%.[1] In many areas of the United States, the levelized cost of electricity from new wind and solar farms is now lower than that from new natural-gas-combined cycle power plants.[2,3] Despite these rapid improvements in the economics of renewable energy sources, their intermittency on both short and long time-scales necessitates energy storage. This can be readily illustrated with comprehensive, current grid information made available by the Energy Reliable Council of Texas (ERCOT), which manages ~90% of the electricity load in Texas.[4] Notably, in that market, wind-capacity alone occasionally exceeds 50% of the total grid load.[4] On top of this substantial wind capacity, by 2022 ERCOT projects that solar capacity will have increased seven-fold compared to 2019 (see Fig. 1a).[4] As shown in Fig. 1b, however,

while the availability of renewable energy is increasing, the load on the electrical grid follows a distinct daily pattern that is decoupled from that of solar and wind output. Furthermore, seasonal variability in the grid-load, as depicted in Fig. 1c, highlights the need for longer duration storage, over months or even years.[2] As such, energy storage with sufficient capacity and the flexibility to level these short and long-term intermittencies is a vital component of the nascent, renewable energy portfolio.

Among several technologies under development to meet the storage needs of a modern, sustainable electrical grid, redox flow batteries (RFBs) have received considerable recent interest.[5] A principal advantage of these systems is their uncoupled power and energy ratings, providing them excellent flexibility for a range of stationary storage applications.[6] Seasonal load variations (such as those apparent in Fig. 1c) could be accommodated by high-capacity installations, while simultaneously mitigating short-term, relatively higher power storage requirements (such as those apparent in Fig. 1b). Development of such systems, with capacity for long-duration storage, that can also provide storage for daily cycling, has been identified as an important milestone in achieving zero-carbon electricity goals.[2]

While the majority of RFB systems studied thus far have been based on aqueous electrolytes,[5] the modest electrochemical window in which water is thermodynamically stable to electrolysis has led researchers to explore nonaqueous electrolytes.[7] By implementing aprotic solvents, nonaqueous redox

ªDepartment of Chemistry and Biochemistry, University of Massachusetts Dartmouth, MA 02747-2300, USA. E-mail: pcappillino@umassd.edu

ᵇDepartment of Mechanical Engineering, Energy Engineering Graduate Program, University of Massachusetts Lowell, Lowell, MA 01854, USA
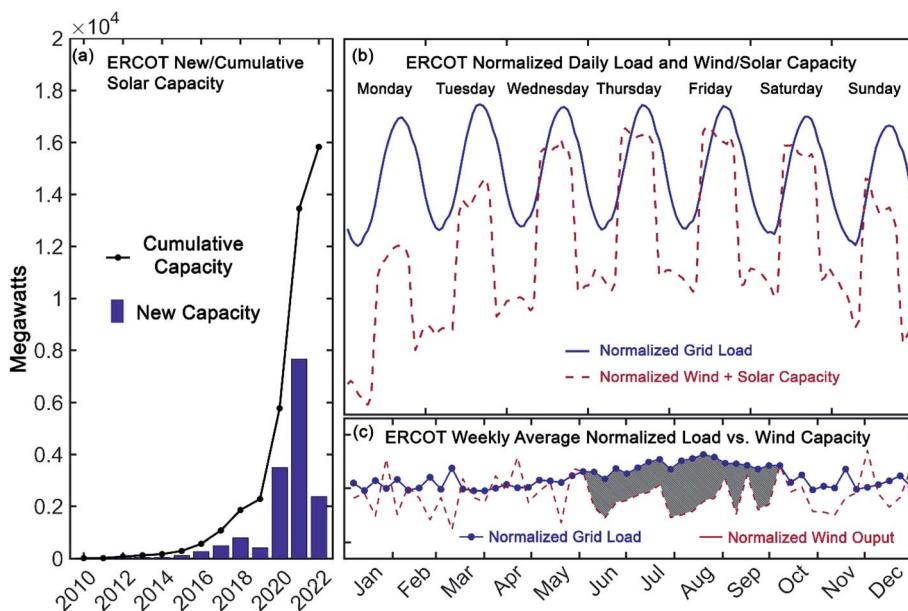
Fig. 1 New (bar) and cumulative (line) solar capacity reported by ERCOT (a), normalized grid load and renewable capacity in Texas for July 15–21, 2019 (load and wind) and July 13–19, 2020 (solar) (b), and weekly average normalized grid load and wind output in Texas during 2019 (shaded region highlights the increased grid load during summer months) (c). Data provided by the Energy Reliability Council of Texas in ref. 4.

flow batteries (NRFBs) expand the thermodynamic potential window at which a flow battery may operate.[8] Notwithstanding kinetic stabilization of aqueous systems,[9] which allow for metastable electrolytes, if an appropriate NRFB chemistry can be elucidated the energy density of flow batteries could be greatly improved. The need for robust, high energy-density active materials for NRFB electrolytes has led to investigation of an array of organic[7,10–21] and metalorganic[7,9,14,22–29] redox couples, as well as redox polymers.[7,14,30,31] While a recent techno-economic analysis concludes that a pathway exists to cost-effective energy storage based on NRFB, thus far, poor chemical stability, leading to low cyclability and low solubility are key remaining research challenges that have prevented implementation of this technology.[32]

Recently, a catholyte was reported that meets the challenging chemical-stability requirements of an NRFB system by using a molecule that is produced biologically, rather than one elucidated by human-design.[33] Biosynthesis of the vanadium compound known as Amavadin (see Fig. S1†) evolved naturally in mushrooms from the *Amanita* genus, under selection pressure for strong and specific vanadium binding, resulting in the most stable vanadium species that has been reported to date.[33] The analogous, dianionic coordination compound, vanadium(4^+) bis-hydroxyiminodiacetic acid ([VBH]) can be synthesized at large scale, using inexpensive reagents and exhibits high chemical stability, even under cycling at high current and to deep states-of-charge.[34] This stability provides a robust system with which to explore the deep parameter space of solvents, salts and cell components that make NRFBs such an attractive frontier for energy storage research.

Herein we report a breakthrough in the design and synthesis of VBH-based NRFB active-materials that greatly improves on

their solubility, which is recognized as a critical parameter in determining energy density,[32,35] and demonstrates their potential as a scaffold for development of next-generation flow battery electrolytes. These gains are supported by electronic structure calculations and placed in a theoretical framework that considers active material solubility (S_{VBH}), resulting from the interplay between two thermodynamic quantities: the free-energy of active-material/solvent interactions (ΔG_{sol}^*, Fig. 2) and free-energy of the active-material crystal lattice (ΔG_{lat}^*, Fig. 2).[35–37] This framework provides a design-strategy for further gains in VBH solubility and lays a blueprint for tuning
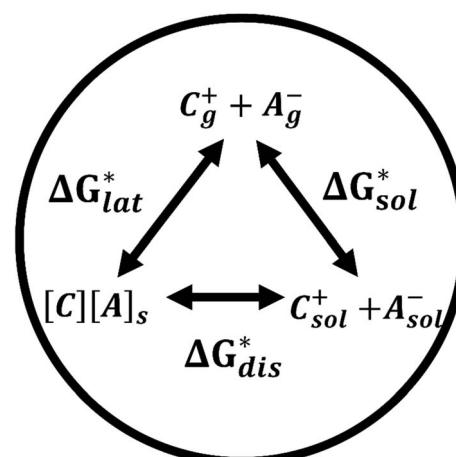
**Fig. 2** Schematic representation of the thermodynamic cycle for dissolution of [cation][VBH] complexes. The free-energy of dissolution (ΔG_{dis}^*) determines the solubility of the complex and results from the interplay between the free-energy of the lattice (ΔG_{lat}^*) and that of stabilizing solute–solvent interactions in solution (ΔG_{sol}^*).

$$CaVBH \text{ (s)} + 2[\text{Cation}][\text{Fluoride}] \text{ (sol)} \rightarrow CaF_2 \text{ (s)} + [\text{Cation}]_2[VBH] \text{ (sol)}$$

N_{1111} N_{2222} N_{3333} N_{4444}
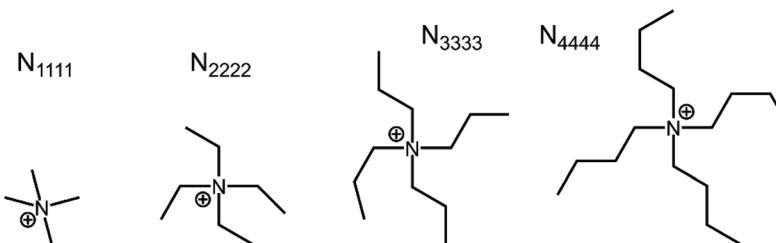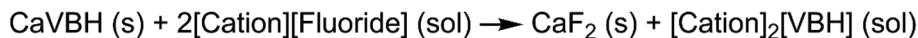
Fig. 3 Scheme for preparation of arbitrary cations of [VBH] by metathesis of the calcium ion. N_{XXXX}, $X = 1$, 2 3 and 4 correspond to the tetramethylammonium, tetraethylammonium, tetrapropylammonium, and tetrabutylammonium cations, respectively.

VBH concentration in various electrolyte compositions. Crucially, electrochemical studies, also reported herein, demonstrate that VBH maintains high stability in concentrated electrolytes during cycling to deep state-of-charge, over an extended duration.

Results and discussion

[VBH] cation metathesis

While the calcium(2^+) salt of [VBH] (CaVBH) can be conveniently prepared at large scale, with high yield, this compound exhibits low solubility in all solvents investigated.[33,34] We reasoned that replacing the calcium ion with alkylammonium cations would significantly alter solubility (S^*_{VBH}) by affecting solute–solvent interactions in the electrolyte as well as anion–cation interactions in the crystalline solid. The thermodynamics of active-material dissolution are governed by the following equation:[35–37]

$$\Delta G^*_{dis} = \Delta G^*_{lat} + \Delta G^*_{sol} = -RT \ln\left(S^*_{VBH} \times V_m\right) \quad (1)$$

In this equation, S^*_{VBH} refers to the molar solubility of a [cation][VBH] complex, ΔG^*_{dis} refers to the free-energy of dissolution of the complex, ΔG^*_{lat} refers to the lattice free-energy of the complex, ΔG^*_{sol} refers to the free-energy of solute–solvent interaction, and V_m is the molar volume of solid [cation][VBH]. To systematically probe these quantities, a strategy to replace calcium (2^+) with arbitrary cations was devised, in which CaVBH is treated with the fluoride salt of the targeted cations (see Fig. 3). After filtration to remove the insoluble fluorite salt, this
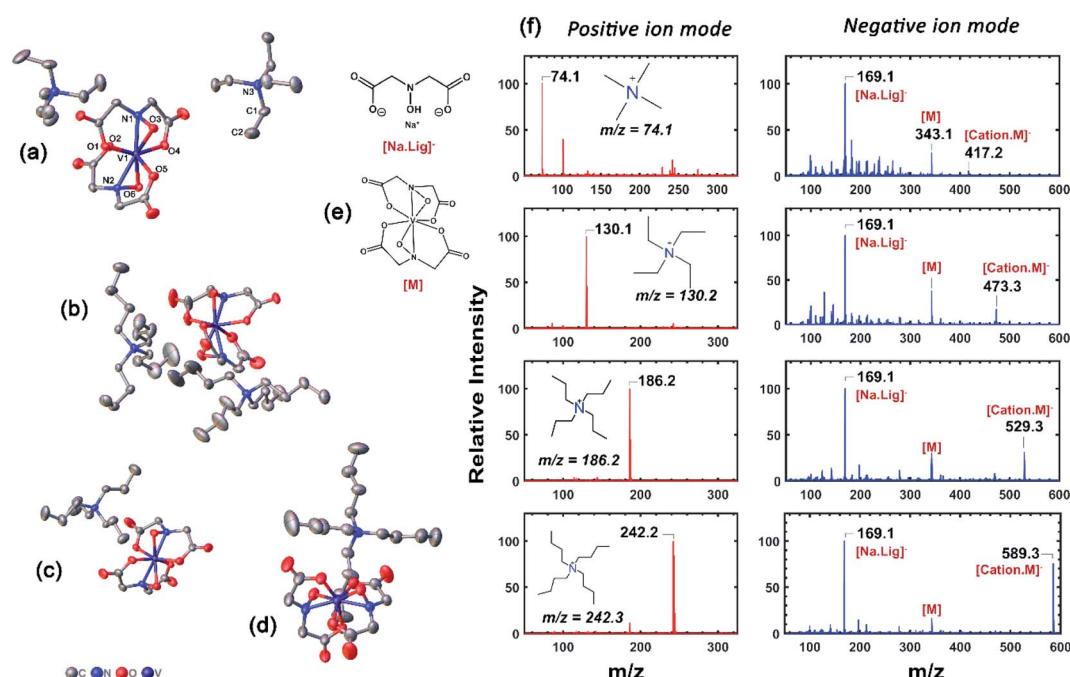
Fig. 4 X-Ray crystallographic data, and mass spectrometric characterization of [N_{XXXX}]$_{1,2}$[VBH]. (a) and (b) correspond to thermal ellipsoid plots of N_{2222} and N_{4444}, bis-alkylammonium, vanadium(4^+) [VBH], respectively and (c) and (d) correspond to those of N_{3333} and N_{4444} mono-alkylammonium, vanadium(5^+) [VBH], respectively. Structures of key ions present in the mass spectrometry are provided in (e) and (f) corresponds to the positive and negative mode mass spectra of [N_{XXXX}]$_2$[VBH], $X = 1$ to 4. Further details of X-ray crystallographic measurements can be found in ESI.†

solution can be used directly as a battery electrolyte or the [cation][VBH] salt can be isolated as a solid. This strategy was used to prepare a series of symmetric, bis-alkylammonium salts of [VBH], having from one to four methylene units in the alkyl groups adjacent to the central nitrogen atom (N_{XXXX}, where X = 1–4 methylene units (see Fig. 3). Removal of solvent affords crystals of alkylammonium [VBH] compounds suitable for X-ray crystallography (see Fig. 4a, and b). Further, chemical oxidation of the vanadium(4^+) species, $[N_{3333}]_2$[VBH] and $[N_{4444}]_2$[VBH], allows preparation of the oxidized, vanadium(5^+) species, as characterized by X-ray crystallography (see Fig. 4c and d, respectively). Mass spectrometry indicates the presence of the parent [VBH] ion in solution as well as monocation adducts (see Fig. 4e and f).

In addition to the X-ray crystallography and mass spectrometry discussed above, ^{1}H NMR spectroscopy provides insight into the structure of the [VBH] active-materials. Integration of the ^{1}H spectra of $[N_{3333}]$[VBH] and $[N_{4444}]$[VBH] (see Fig. 5) exhibits ratios of [VBH]-methylene protons to alkylammonium–methylene and –methyl protons of ~8 : 8 : 8 : 12 and 8 : 8 : 8 : 8 : 12, respectively, confirming the expected stoichiometries of the ions. In both compounds, the methylene region of the spectra, between ~4.3 and 5 ppm contains eight peaks which can be assigned to four sets of equivalent protons of the [VBH] ligands, each split by a strongly coupled, geminal proton ($^2J_{HH}$ = 16 Hz).[38,39] DFT-predicted NMR shifts (see Fig. 5, inset) aid in assigning these peaks, with the two protons in the same face as the η^2-NO ligand (H_3 and H_4, Fig. 5) up-field

compared to the protons on the opposite face (H_1 and H_2, Fig. 5) as a result of shielding from a more electron-rich quadrant of the coordination sphere. These four ligand proton positions are related to another set by a C_2 operation through the vanadium center (see Fig. 5). This description is roughly consistent with the assignment reported for the natural product Amavadin,[40] which contains two chiral methine positions in each ligand, in place of the methylene positions in [VBH].

Solubility of alkylammonium [VBH] compounds

Metathesis of the calcium(2^+) ion in the manner described above and depicted in Fig. 3 profoundly affects the solubility of the [cation][VBH] active-materials. As shown in Table 1, CaVBH is insoluble in all solvents tested except for water and DMSO, in which it is modestly soluble. A clear trend emerges, in which VBH exhibits increasing solubility with increasing alkyl-chain-length. It is also notable that the oxidation state of the cation plays an important role in solubility, with the reduced, dianionic species exhibiting greater solubility (*vide infra*). Formulation of NRFB electrolytes containing active-material and support cation with concentrations approaching one and two mol L^{-1}, respectively, constitutes a significant milestone. Careful consideration of these solubility trends and casting them in the context of a more general theoretical framework, has the potential to lead to further improvements and provides general insight into the development of high-energy density NFRB electrolytes.

Thermodynamic considerations for [cation][VBH] solubility

Solubility trend in the steric bulk of the [VBH]$^{2-}$ counter-cation(s). To better understand the solubility trends discussed above, DFT calculations were performed on the alkylammonium cations and the VBH anions using their crystal structures as input geometries.[35] As noted by Thompson *et al.*,[35] calculation of solvation energy ΔG^*_{sol} (see Fig. 2), or the difference between gas-phase and solvated ions, is straightforward and the values for each of the $[N_{XXXX}]_y$[VBH] species (y = 1 or 2 for oxidized and reduced active-material, respectively) for which solubility data has been measured is listed in Table 2. These calculations were carried out using a model known as SMD,[41] in which the solvent is considered a continuous dielectric medium[42] interacting with the solute electron density. This model accounts for electrostatic interactions of a polarizable continuum stabilizing the permanent charges on the cation and anions, as well as short-range dispersion interactions between the solvent and solute molecules in the first solvation shell (see Fig. 6a).[41] Interestingly, the trend in ΔG^*_{sol} runs counter to the experimentally observed solubility data. Electrostatic potential plots, shown in Fig. 6, prepared using natural charges output from natural bond orbital analysis,[43] provide an explanation for this effect based on the distribution of positive charge on each cation. In all four cases (N_{XXXX}, X = 1–4) the central nitrogen and carbon atoms are relatively electroneutral while the bulk of the positive charge is concentrated on the protons bonded to the carbon directly adjacent to the nitrogen atom. This effect is readily apparent in the ^{1}H-NMR spectroscopy of the alkylammonium ions (see Fig. 5), with a large downfield shift of the
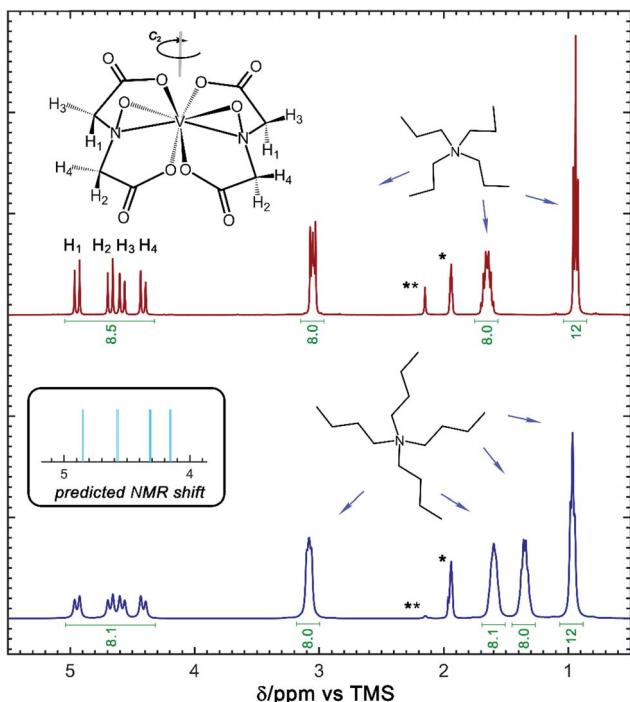

Fig. 5 NMR spectra of the vanadium(5^+) complexes of $[N_{3333}]$[VBH] (top, red) and $[N_{4444}]$[VBH] (bottom, blue). Insets show the stick diagram and predicted NMR chemical shifts of the [VBH] anion, as well as the stick diagrams of the $[N_{3333}]$ and $[N_{4444}]$ cations.

Table 1 Solubility of $[N_{XXXX}]_y[VBH]$ active-materials in various solvents, $X = 1$ to 4, $y = 1$ for vanadium(5^+) species and $y = 2$ for vanadium(4^+) species. Values correspond to the maximum concentration of [VBH] in the electrolyte in mol L^{-1}, as determined by UV-Vis spectroscopy. Values of dielectric constant taken from ref. 42

Solvent	Dielectric constant	Vanadium(4^+) species					Vanadium(5^+) species	
		$[Ca]^{2+}$	$[N_{1111}]_2^+$	$[N_{2222}]_2^+$	$[N_{3333}]_2^+$	$[N_{4444}]_2^+$	$[N_{3333}]^+$	$[N_{4444}]^+$
Tetrahydrofuran	7.5	Insoluble	Insoluble	Insoluble	Insoluble	0.17	Insoluble	0.008
Acetonitrile	37	Insoluble	0.004	0.33	1.09	0.80	0.12	0.51
Dimethylsulfoxide	47	0.54	0.11	0.53	0.83	0.69	0.62	0.55
Propylene carbonate	66	Insoluble	0.03	0.28	0.68	0.77	0.27	0.65

methylene protons adjacent to the nitrogen atom. These electropositive protons become less solvent-accessible as the alkyl-chain lengthens, preventing stabilizing dipole interactions between the solute and the solvent continuum and resulting in a less negative ΔG^*_{sol}.

Considering the trend in solvation energies of the alkyl-lammonium species discussed above, it is clear that any meaningful theoretical prediction of active-material solubility must account for the lattice energy of the solid, at least qualitatively. Furthermore, the experimentally observed trend of steeply increasing solubility for $[N_{XXXX}]_y[VBH]$ with increasing

Table 2 DFT-calculated solvation energies (ΔG^*_{sol}) for reduced and oxidized $[N_{XXXX}]_y[VBH]$ compounds in acetonitrile, $X = 1$ to 4, and $y = 2$ for reduced species and $y = 1$ for oxidized species

Vanadium(4^+)	ΔG^*_{sol}/kJ mol^{-1}	Vanadium(5^+)	ΔG^*_{sol}/kJ mol^{-1}
$[N_{1111}]_2[VBH]$	-1111	$[N_{1111}][VBH]$	-477
$[N_{2222}]_2[VBH]$	-1065	$[N_{2222}][VBH]$	-454
$[N_{3333}]_2[VBH]$	-1049	$[N_{3333}][VBH]$	-446
$[N_{4444}]_2[VBH]$	-1054	$[N_{4444}][VBH]$	-449
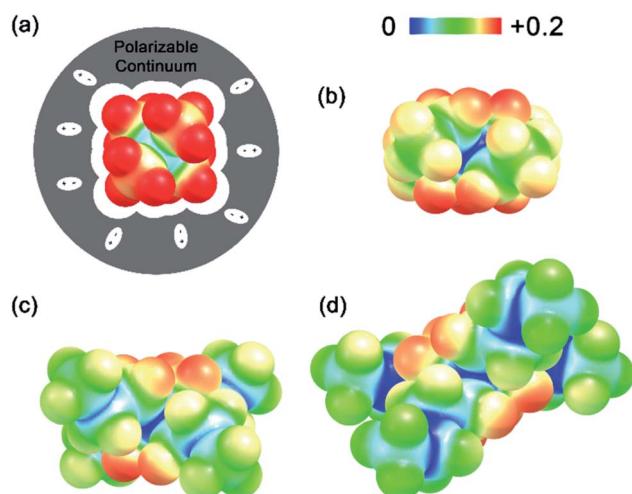
alkyl-chain length must arise from destabilization of the crystal lattice. This is in accord with reported values of lattice energy for alkylammonium halides derived from thermochemical measurements, which show less negative lattice energy with longer alkyl-chain substituents.[44-46] This observation also resonates with the observed high solubility of so-called non-coordinating anions, which is explained by low lattice energy inherent to bulky anions.[47] Shown schematically in Fig. 7, with increasing alkyl-chain length, the effect of lattice destabilization (ΔG^*_{lat}) overcomes the destabilization of the solvated ions (ΔG^*_{sol}), resulting in an overall more negative ΔG^*_{dis}, thus a higher solubility (S^*_{VBH}, eqn (1)) for the bulkier cations. Notably, the solubility of CaVBH in DMSO, which is higher than that of $[N_{1111}]_2[VBH]$ and comparable to $[N_{2222}]_2[VBH]$, is an outlier in the trends discussed above. This may be the result of specific solute–solvent interactions not captured in the continuum model used, or atypical thermodynamic properties of its crystal lattice. While no theoretical framework could account for all possible physical properties of a real system, the high solubility of CaVBH in DMSO underscores the importance of a predictive theoretical framework, not to facilitate rational electrolyte design but also to identify potentially valuable outliers.

Solubility trend for the oxidized, $[VBH]^{1-}$ species. A cycling flow battery must comprise stable electrolytes in both oxidation


Fig. 6 Electrostatic potential maps plotted using natural charges of N_{1111}, N_{2222}, N_{3333} and N_{4444} cations (a–d respectively). Gray-shaded region represents the polarizable continuum used by the SMD method.
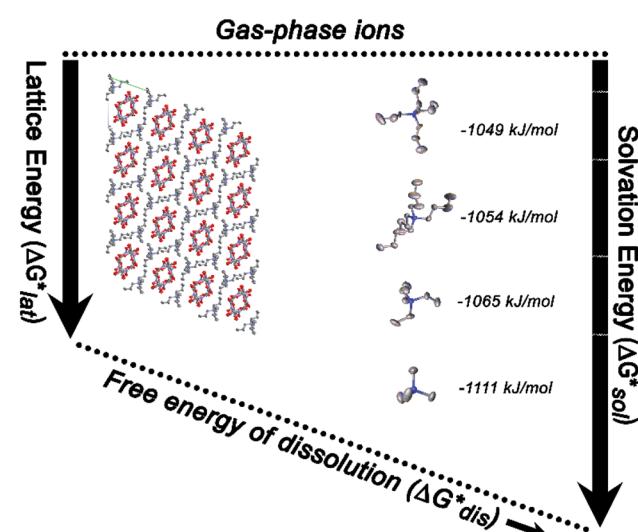

Fig. 7 Thermodynamic cycle for dissolution of VBH compounds of N_{1111}, N_{2222}, N_{3333} and N_{4444} cations.

states of the active-materials. As such, additional insights were gained by measuring the solubility of oxidized, $[N_{3333}][VBH]$ and $[N_{4444}][VBH]$ (Table 1) and these were incorporated into the theoretical framework discussed above.

First, compared to reduced, $[VBH]^{2-}$, one would expect oxidized, $[VBH]^{1-}$ would exhibit a less stable crystal lattice (*i.e.*, less negative ΔG_{lat}^*), due to the decreased overall charge of the complex.[48] A destabilized lattice should have the effect of increasing solubility upon oxidation. Second, with respect to the free energy of the solvated ions (ΔG_{sol}^*), the loss of one cation, and the decreased charge on the anion should result in a less stable solution (less negative ΔG_{sol}^*) for the oxidized, VBH^{1-} complex compared to the reduced, $[VBH]^{2-}$ species. This agrees with the DFT-calculated values of ΔG_{sol}^* for the oxidized complexes (Fig. 8), which are less negative by 620–650 kJ mol^{-1} in the oxidized state. A destabilized solution should have the effect of decreasing solubility. Taken together with the experimentally observed solubility, (see Table 1), several conclusions can be drawn:

- Upon oxidation of $[VBH]^{2-}$, the positive change in ΔG_{sol}^* upon oxidation is greater than the positive change in ΔG_{lat}^*, otherwise the active-material would become more soluble, not less.

- Since the change in ΔG_{sol}^* upon oxidation of $[N_{3333}]_2[VBH]$ and $[N_{4444}]_2[VBH]$ is nearly identical (~620 kJ mol^{-1}), and considering $[N_{3333}][VBH]$ is much less soluble than $[N_{4444}][VBH]$, the positive change in lattice energy upon oxidation must be less for $[N_{3333}]_2[VBH]$ than for $[N_{4444}]_2[VBH]$.

- Since the solubility of oxidized, $[N_{4444}][VBH]$, is similar to that of reduced, $[N_{4444}]_2[VBH]$, the change in lattice energy similar to the change in solvation energy, on the order of 600 kJ mol^{-1}.

In summary, the increase in solubility observed for VBH compounds with longer-chain alkylammonium cations comes

as a result of lattice destabilization and despite a less favorable solvation energy. Further, ΔG_{sol}^* and ΔG_{lat}^* change upon oxidation, and in some cases are close in magnitude. Detailed computational investigations of the lattice enthalpy of these compounds is currently underway to identify structural aspects of the cation and VBH that may be changed to destabilize ΔG_{lat}^* and increase solubility. Finally, by considering the variability of ΔG_{sol}^* for oxidized and reduced VBH-complexes with various cations and in several solvents (see Fig. 8) we demonstrate that a pathway exists to optimize both thermodynamic quantities for solubility by altering cation and anion structure, as well as by altering the dielectric constant of the solvent/solvent mixture used to formulate the electrolyte.

Electrochemical characterization of high-concentration VBH electrolytes

A critical aspect of improving solubility of VBH electrolytes is maintaining high stability and cyclability by avoiding deleterious side-reactions that may become more severe at high concentrations. As shown in Fig. 9a, $[N_{4444}]_2[VBH]$ can be cycled exhaustively at 0.24 mol L^{-1} to high depth-of-charge (DOC) with no chemical decomposition, as monitored by UV-Vis spectroscopy. After 16 round-trip cycles, comprising two initial and two final cycles between 90% and 10% DOC, with intervening cycles between 60% and 40% DOC, virtually no chemical decomposition of the active-material was observed. Subsequently, electrolyte solutions were remixed and cycled for an additional 6 cycles without observable decomposition. Notably, these experiments took place over the course of more than one week of constant cycling. As shown in Fig. 9b–g, the vanadium(4$^+$) and vanadium(5$^+$) concentrations at each electrode can be extracted by simulating the observed spectrum as a linear combination of the reference spectra (see Fig. S2†). The spectroscopic signatures of the electrolytes are identical before and after the experiment and the total VBH concentration was unchanged after 183 h of galvanostatic cycling at between 5 and 8 mA. The long duration of each cycle, due to high area-specific resistance, prevented investigation of active material-concentrations near the limit of their solubility. We expect that higher concentration studies will be more feasible at higher current density, in a flow cell architecture.

Kinetics of high-concentration reduced/oxidized VBH by ultramicroelectrode voltammetry

In addition to exhaustively cycling high-solubility VBH electrolytes, the kinetic behavior of these electrolytes at high concentrations was investigated. Cyclic voltammetry (CV) is a useful tool to explore the fundamental electrochemical properties of the electrolyte at low active-material concentrations using Randle–Sevcik and Butler–Volmer theoretical models. However, at higher concentrations, uncompensated resistances would result in a deviation from the linear relationship, leading to inaccurate predictions of the intrinsic electrochemical properties.[49,50] To eliminate this problem, a carbon fiber ultramicroelectrode (UME) was used to probe the redox reactions at near-iR-free conditions.[50] Fig. 10 shows steady-state
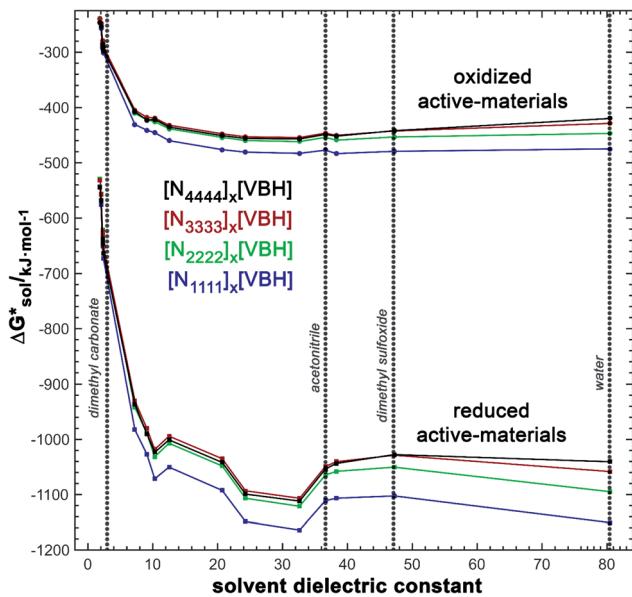

Fig. 8 DFT-calculated values of ΔG_{sol}^* for reduced and oxidized $[N_{XXXX}]_Y[VBH]$ compounds in various solvents with dielectric constant varying between 2 and 80 ($X = 1$ to 4, and $Y = 2$ for reduced species and $Y = 1$ for oxidized species).
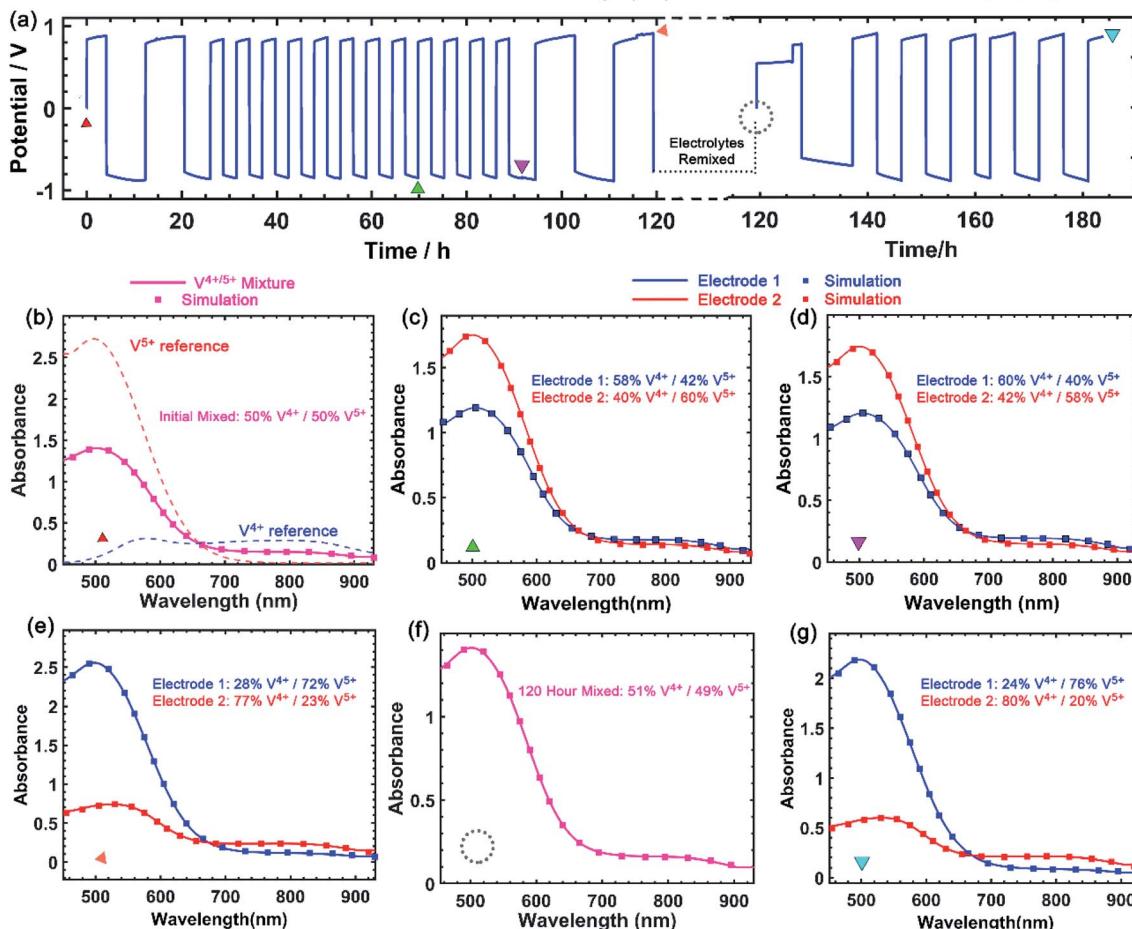
Fig. 9 Electrochemical cycling of 0.24 mol L^{-1} [VBH] solution in MeCN, over the course of more than 180 hours, comprising 22 roundtrip cycles of 80% and 20% DOC (a). Panels (b)–(g) correspond to UV-Vis traces and simulated traces used to determine concentration of VBH in the reduced and oxidized states at the time point indicated by symbols in panel (a). Data were collected with a 20 mL 2-electrode cell with double-sided MPL carbon cloth (12.9 cm^2) current collector, with between 5 and 9 mA of current.

voltammograms of both reduced and oxidized forms of [N$_{4444}$]$_2$VBH in MeCN and the corresponding kinetic parameters are summarized in Table 3. As expected, the exchange current density increases and the diffusion coefficient decreases with increasing [N$_{4444}$]$_2$VBH concentration, while the observed rate constant decreases slightly. Although the oxidized form of VBH
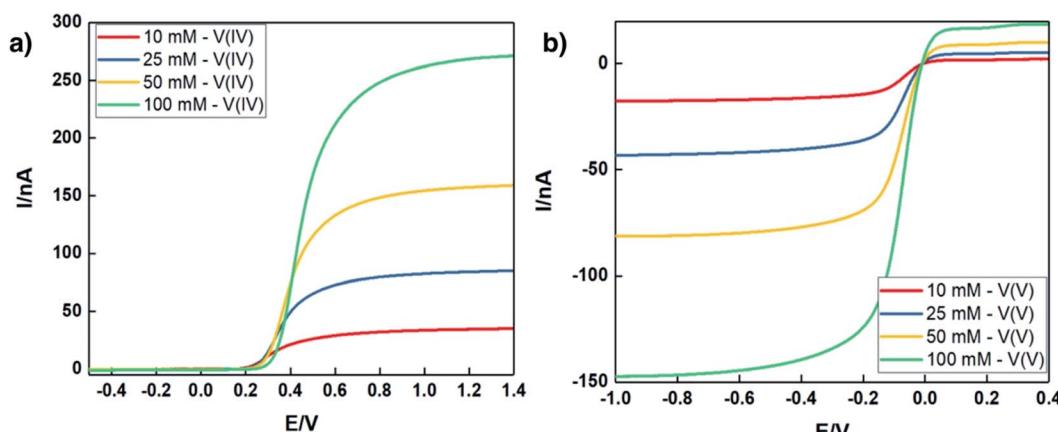
Fig. 10 Steady state voltammograms of (a) reduced form, (b) oxidized form of [N$_{4444}$]$_2$VBH in MeCN at a scan rate of 0.05 V s^{-1}. All experiments were performed using a carbon fiber UME at room temperature (25 °C).

Table 3 Electrochemical parameters of VBH electrolytes in MeCN, obtained using UME voltammetry, with j_0 as exchange current density, k_0 as standard rate constant and D_0 as the diffusion coefficient

	Reduced form – $[VBH]^{2-}$			Oxidized form – $[VBH]^{1-}$		
Conc. [M]	j_0 [mA cm^{-2}]	$k_0 \times 10^{-3}$ [cm s^{-1}]	$D_0 \times 10^{-6}$ [cm^2 s^{-1}]	j_0 [mA cm^{-2}]	$k_0 \times 10^{-3}$ [cm s^{-1}]	$D_0 \times 10^{-6}$ [cm^2 s^{-1}]
0.010	10.6	10.9	15.1	5.01	5.2	8.29
0.025	27.5	5.69	7.97	14.3	2.96	4.04
0.050	46.9	4.86	7.00	29.6	3.07	3.78
0.100	108	5.61	6.08	48.8	2.53	3.49

electrolytes exhibit lower electrochemical rate constants in comparison to the reduced form due to increased viscosity (see Fig. S3.†), this UME analysis demonstrates that high-solubility VBH electrolytes exhibit fast electron transfer kinetics with rate constants in the range of 10^{-2}–10^{-3} cm s^{-1}.[51,52]

Conclusion

The increased solubility reported herein is an inroad to overcoming a major obstacle to formulation of high energy-density NRFB electrolytes with VBH-based active-materials. These systems have the potential to address a growing need for flexible, robust grid energy storage systems. In addition, the insights developed herein provide a framework for electrolyte optimization. Future efforts will focus on tailoring electrolyte thermodynamics with combined theoretical and experimental approaches and assessing flow cell performance using electrolytes with high active-material concentrations.

Experimental

General

Tetraethylammonium fluoride hydrate (TEAF, 97%), tetra-n-propylammonium chloride (TPACl, 99%), chloroacetic acid (HClOAC, 98%), vanadium(IV) oxide acetylacetonate, and anhydrous potassium fluoride (KF, 99%) were purchased from Bean Town Chemicals. Tetra-n-butylammonium fluoride hydrate (TBAF) and tetra-n-butylammonium hexafluorophosphate (TBAPF$_6$) were purchased from Oakwood Chemicals. TBAPF$_6$ was recrystallized from ethanol twice prior to use. Hydroxylamine hydrochloride (NH$_2$OH·HCl, 99%) was purchased from Alfa Aesar. Zinc acetate dihydrate, 97% was purchased from Acros Organics. Tetramethylammonium fluoride tetrahydrate (TMAF, 98%) was purchased from Matrix Scientific. Calcium chloride dihydrate was purchased from VWR. Ferrocenium hexafluorophosphate, 97% was purchased from Sigma Aldrich. All chemicals were used as obtained unless mentioned otherwise. All solvents were obtained from Fisher Scientific, distilled over drying reagent and stored in a nitrogen-filled glovebox with oxygen and moisture content less than 1 ppm.

Physical methods

UV-Vis spectra were collected in a Evolution 220 UV-visible Spectrophotometer (Thermo Scientific) using a quartz cuvette of 1 cm path length. Calibration curves (see Fig. S4 and S5.†) were drawn to estimate the molar absorptivity of VBH^{1-} (reduced) and VBH^{2-} (oxidized) at 825 nm and 485 nm respectively. The total concentration and fraction of each redox state of active material during cell cycling were estimated by simulating the observed spectra as a linear combination of reference spectra. Infrared spectra were recorded on a Thermo Scientific Nicolet iS5 equipped with iD7ATR module and a diamond crystal. ^{1}H- and ^{13}C-NMRs were recorded on Bruker AVANCE III HD 400 MHz High-Performance Digital NMR spectrometer operating at 400 MHz for ^{1}H NMR, and 101 MHz for ^{13}C NMR. Data acquisition was performed on IconNMR 5.0.3, and spectra were processed in TopSpin 3.5 and Mnova. High Resolution Mass Spectrometry (HRMS) were recorded on a Waters Xevo QTOF-I spectrometer using direct infusion-electrospray ionization technique. X-ray crystallographic experiments were performed on a Bruker D8 Venture X-instrument, using Mo Kα radiation at 200 K. Data were corrected for absorption using SADABS. The structures were solved by direct methods. All non-hydrogen atoms were refined anisotropically by full matrix least squares on F² and all hydrogen atoms except those on water were placed in calculated positions with appropriate riding parameters. Further refinement and molecular graphics were obtained using Bruker Suite of structural programs,[53] and OLEX2.[54]

Electrochemical methods

All electrochemical experiments were carried out in N$_2$-filled glovebox with oxygen and water content less than 1 ppm.

Cyclic voltammetry was performed in a custom designed cell. Working electrode was 2 mm diameter glassy carbon electrode. Platinum wire was used as counter electrode. Nonaqueous reference electrode was fabricated by submerging a piece of silver wire in 25 mM silver nitrate solution in acetonitrile with 0.1 M TBAPF6 in a glass tube fitted with vycor frit on one end. CV and charge discharge experiments were recorded using Ametek VersaSTAT3 (Princeton Applied Research).

Ultramicroelectrode (UME) voltammetry: analysis of the redox reaction kinetics in high-concentration VBH electrolytes was performed with a UME voltammetry setup. 11 μm-diameter carbon fiber UME (BASi) was used as the working electrode. Platinum wire and silver wire were selected as counter and reference electrodes, respectively. The working electrode was prepared by rinsing the 11 μm carbon fiber with DI H$_2$O,

polishing with 0.05 μm alumina suspension, and then rinsing a second time with DI H_2O. The reference electrode was calibrated against ferrocene in the respective support electrolyte. 5 mL of electrolyte were used for all UME experiments.

The standard rate constants (k^0) were calculated according to the Butler–Volmer equation:

$$k^0 = \frac{I_0}{nFAC}$$

where I_0 is exchange current (A), n is the number of electrons, F is the Faraday constant (96485 C mol^{-1}), A is the electrode area, and C is the active species concentration (mol cm^{-3}). Quantitative analysis of diffusion coefficients (D_0) of was derived from the steady-state current plateau of the UME voltammograms. The steady-state current is used to calculate D_0 using the following relationship:

$$i_{ss} = 4FrD_0nC$$

where F is Faraday constant and r is the radius of the electrode (5.5 μm). C indicates the concentration of redox materials.

Galvanostatic charge discharge cycling was conducted with a two-electrode cell setup in a 20 mL H-cell from Adams and Chittenden Scientific. Double sided MPL carbon cloth (12.9 cm^2) was used as electrode. Nafion membrane was soaked in solution of 0.5 M TBAPF6 in MeCN for 24 h prior to use.

Solubility of alkylammonium [VBH] compounds

Solubilities were experimentally measured by UV-Vis absorbance spectroscopy at room temperature, based on calibration curves (see Fig. S4 and S5.†). Saturated solutions of each of the compounds were made in the four different solvents and centrifuged. Samples were then diluted for measurement.

Synthetic methods

Ligand synthesis. Zinc(2$^+$) hydroxyiminodiacetate (ZnHIDA) was synthesized using literature method[55] with modification as follows. Hydroxylamine hydrochloride (70.1 g, 1.01 mol) was neutralized with 5 M NaOH (200 mL, 1.00 mol) in an ice bath while maintaining the temperature of the reaction mixture below 4 °C. In another flask, chloroacetic acid (189 g, 2.00 mol) was slowly neutralized with 5 M NaOH (400 mL, 2.00 mol) in an ice bath. Neutralized solution of chloroacetic acid was then added dropwise to hydroxylamine solution. An additional 400 mL 5 M NaOH solution was added to the reaction mixture and was stirred for 72 h in an ice bath. The reaction mixture was then and acidified to pH 3.9 by adding 6 M HCl. Zinc acetate dihydrate (220 g, 1.00 mol) was then added to the solution while stirring. White precipitate of ZnHIDA was filtered and washed with cold water several times and dried *in vacuo*. Yield: 201 g, 0.948 mol, 95%. IR (ν/cm^{-1}): 3228w, 2930w (C–H), 1648 m, 1576s (C=O).

Synthesis of active materials. CaVBH was synthesized using a modification of literature procedures[55] with slight modification for scale up. ZnHIDA (83.2 g, 0.392 mol) was added to 500 mL de-ionized water to which vanadyl(4$^+$)acetylacetonate (52.0 g, 0.196 mol) was added and mixed well using magnetic stirrer. Hydrochloric acid (80.0 mL, 6.0 M) was added dropwise to the mixture with stirring until dissolution of all the reactants occurred. Calcium chloride dihydrate (28.8 g, 0.197 mol) was added to the mixture and dissolved. CaVBH was precipitated from resulting dark blue solution by addition of 2 L of isopropanol. The product was filtered and washed with 20 mL isopropanol followed by acetone and dried *in vacuo* for 24 hours at room temperature. (Yield: 78.87 g, 0.167 mol, 85%) UV-Vis (DMSO): λ_{max} = 578 nm (ε = 27.5 mol^{-1} cm^{-1}). IR (ν/cm^{-1}): 3541w, 3321w, 2988w, 1589 s (C=O).

[(N$_{1111}$)$_2$VBH]. CaVBH (4.32 g, 0.00913 mol) was added to stirring mixture of tetramethylammonium fluoride tetrahydrate (3.01 g, 0.018 mol) in 50 mL ethanol. The reaction mixture was stirred at 30 °C for 1 h. The solution of [(N$_{1111}$)$_2$VBH] in ethanol was isolated by centrifuging mixture at 3000 rpm for 10 min and concentrated using a rotatory evaporator. Crystals were obtained by cooling the solution in an ice bath, collected *via* vacuum filtration, and dried in *vacuo* for 16 h at room temperature. (Yield: 3.40 g, 0.00607 mol, 66%) Single crystals suitable for X-ray analysis were obtained by diffusing THF into solution of compound in ethanol. UV-Vis (DMSO): λ_{max} = 579 nm (ε = 30.2 mol^{-1} cm^{-1}). IR (ν/cm^{-1}): 3345w, 3031w, 2962w (C–H), 1619s (C=O), 1492w (C–N). HR-MS (ESI, positive ion mode) m/z calculated for $C_4H_{12}N^+$ [M]$^+$: 74.0964, found: 74.0954.

[(N$_{2222}$)$_2$VBH]. CaVBH (9.60 g, 0.0203 mol) was added to solution of tetraethylammonium fluoride (6.11 g, 0.0409 mol) in 60.0 mL acetonitrile and stirred overnight at room temperature. CaF_2 precipitate was separated by vacuum filtration and the filtrate volume was reduced to *ca.* 20 mL in a rotatory evaporator which on cooling yielded blue crystals. Product was separated, washed with cold THF and dried *in vacuo*. (Yield, 11.3 g, 0.0182 mol, 90%). UV-Vis (MeCN): λ_{max} = 578 nm (ε = 28.2 mol^{-1} cm^{-1}). IR (ν, cm^{-1}): 3506w, 2994w, 2955w, 2909w, 1602s (C=O). HR-MS (ESI, positive ion mode) m/z calcd for $C_8H_{20}N^+$ [M]$^+$: 130.1590, found: 130.1554.

[(N$_{3333}$)$_2$VBH]. [(N$_{3333}$)$_2$VBH] was synthesized in the same manner as [(N$_{1111}$)$_2$VBH], using CaVBH and tetrapropylammonium fluoride (TPAF). Tetrapropylammonium fluoride (TPAF) was prepared by halogen exchange, as reported previously.[56] Tetrapropylammonium chloride (12.7 g, 0.0574 mol) was dissolved in 30 mL dry methanol. KF (4.10 g, 0.0706 mol, 1.25 equ.) and 160 μL water (4% by weight of KF) was added to the solution and the mixture was stirred for 15 min. and filtered. The process was repeated twice and the final filtrate was reduced to volume of *ca.* 7 mL which was filtered to obtain a yellow, oily liquid. A suspension of CaVBH (7.80 g, 0.0165 mol) in 40 mL acetonitrile was prepared to which above yellow oil was added and stirred, resulting in an immediate dissolution of suspended CaVBH. Additional CaVBH (1.50 g, 0.00317 mol) was added to the solution in increments of 0.5 g after which further addition would result in insoluble CaVBH indicating the molar equivalence point. The reaction mixture was centrifuged at 4000 rpm for 15 min. to remove precipitate from the blue liquid. Crystals were obtained by treating the cold solution of the compound with THF which was re-crystalized from MeCN/THF but a sufficiently high-resolution X-ray crystal structure was not obtained due to crystallographic disorder or other crystallographic issue.

(Yield: 14.0 g, 0.0196 mol, 60%). UV-Vis (MeCN): λ_{max} = 579 nm (ε = 27.9 mol^{-1} cm^{-1}). IR (ν, cm^{-1}): 3471w, 2970w (C–H), 2878w, 1607s (C=O), 1488w (C–N). HR-MS (ESI, positive ion mode) m/z calcd for C$_{12}$H$_{28}$N$^+$ [M]$^+$: 186.2216, found: 186.2242.

[(N$_{4444}$)$_2$VBH]. [(N$_{4444}$)$_2$VBH] was prepared in the same manner as [(N$_{1111}$)$_2$VBH], using tetrabutylammonium-fluoride trihydrate (12.9 g, 0.0411 mol) and CaVBH (9.71 g, 0.0205 mol) in 40 mL THF (yield: 14.1 g, 0.0170 mol, 83%). Single crystals were obtained by slow diffusion of diethyl ether into solution of the product in MeCN. UV-Vis (MeCN): λ_{max} = 577 nm (ε = 28.1 mol^{-1} cm^{-1}). IR (ν, cm^{-1}): 3419w, 2957w (C–H), 2872w, 1615s (C=O), 1490w (C–N). HR-MS (ESI, positive ion mode) m/z calcd. for C$_{16}$H$_{36}$N$^+$ [M]$^+$: 242.2842, found: 242.2829.

[(N$_{4444}$)VBH]. [(N$_{4444}$)$_2$VBH] was chemically oxidized to [(N$_{4444}$)VBH] using ferrocenium hexafluorophosphate (FcPF$_6$). In a Schlenk flask [(N$_{4444}$)$_2$VBH] (7.28 g, 0.00880 mol) was dissolved in 30 mL acetonitrile. Suspension of FcPF$_6$ (2.91 g, 0.00879 mol) in acetonitrile was added to the flask and stirred for 15 min. The solution was filtered, and the filtrate was rotovapped to reduce the volume to *ca.* 15 mL. The product was crystallized from acetonitrile/diethyl ether and repeatedly washed with hexane and ether until ferrocene was removed. Red crystalline product was isolated and dried under high vacuum for 24 h. Single crystal suitable for X-ray analysis was obtained by slow diffusion of diethyl ether into solution of the title compound in MeCN (yield: 5.00 g, 0.00855 mol, 97%). UV-Vis (MeCN): λ_{max} = 497 nm (ε = 240 mol^{-1} cm^{-1}). IR (ν, cm^{-1}): 2962w (*C–H*), 2875w, 1667s (*C=O*), 1484w (C–N). δ_H (400 MHz, CD$_3$CN) 4.94 (2H, d, J 16.1), 4.63 (4H, dd, J 38.4, 16.1), 4.41 (2H, d, J 16.1), 3.08 (8H, t, J 7.3), 1.60 (8H, t, J 7.4), 1.35 (8H, q, J 7.2), 0.96 (12H, t, J 7.3). δ_C (101 MHz, CD$_3$CN) 171.00 (d, J 41.3), 65.56 (d, J 67.8), 59.40, 24.38, 20.41, 13.87.

[(N$_{3333}$)VBH]. [(N$_{3333}$)VBH] was prepared by chemical oxidation of [(N$_{3333}$)$_2$VBH] solution in MeCN (14.0 mL, 0.576 M, 0.00806 mol) using FcPF$_6$ (2.66 g, 0.00804 mol). FcPF$_6$ was directly added to the solution and stirred for 30 min. Reddish brown precipitate was isolated and washed with toluene multiple times until trace of ferrocene was removed. Product was recrystallized from a MeCN/diethyl ether mixture. Red powder was isolated *via* filtration and dried in Schlenk line. (Yield 3.90 g, 0.00737 mol, 91%) crystals suitable for X-ray diffraction were grown by vapour diffusion of diethyl ether into acetonitrile solution of the title compound. UV-Vis (MeCN): λ_{max} = 495 nm (ε = 239.88 mol^{-1} cm^{-1}). IR (ν, cm^{-1}): 2968w (C–H), 2880w, 1666s (C=O), 1486w (C–N). δ_H (400 MHz, CD$_3$CN) 4.94 (2H, d, J 16.1), 4.63 (4H, dd, J 38.2, 16.1), 4.41 (2H, d, J 16.1), 3.11–2.97 (8H, m), 1.73–1.56 (8H, m), 0.94 (12H, t, J 7.3).

Computational methods

The solvation free energies (ΔG_{sol}^*) of the +4 and +5 oxidation states of the VBH anion with the corresponding N$_{xxxx}$ (x = 1,2,3,4 is the number of alkyl carbon atoms) alkylammonium cations were investigated over a range of solvent systems (Table S1†).

Implicit solvation was induced using the solvation model based on density (SMD) method implementation in Orca v4.2.1.[57] The Perdew–Burke–Ernzerhof (PBE) generalized gradient approximation (GGA) functional and Grimme's DFT-D3 dispersion correction with Becke–Johnson damping (D3BJ) using the def2-TZVP basis set was used in the equilibrium geometry optimizations in both gaseous and solvated systems.[58–62] The ΔG_{sol}^* for each ion was then taken as the difference between the solvated total energy (E_{sol}) and the gaseous total energy (E_{vac}) (eqn (2)) and corrected for the free energy change ($\Delta G^{0\rightarrow*}$ = 1.9 kcal mol^{-1} at 298 K) associated in converting 1 atm of gas to 1 mol L^{-1} solution (eqn (3)). Eqn (2) holds within the SMD method as this continuum model is parameterized with a substantial dataset of experimental free energies of solvation at room temperature.

$$\Delta G_{sol}^0 = E_{sol} - E_{vac} \qquad (2)$$

$$\Delta G_{sol}^* = \Delta G_{sol}^0 + \Delta G^{0\rightarrow*} \qquad (3)$$

Electrostatic potential plots were prepare using the Multiwfn software package,[63] incorporating natural charges calculated from a natural bond orbital analysis,[43] and cube files were visualized using the Chemcraft software package.[64]

Conflicts of interest

There are no conflicts to declare.

Acknowledgements

References

1 *Sustainable Energy in America Factbook*, https://www.bcse.org/download/, accessed April 11, 19.

2 P. Albertus, J. S. Manser and S. Litzelman, *Joule*, 2020, **4**, 21–32.

3 U. S. E. I. Administration, *Levelized Cost and Levelized Avoided Cost of New Generation Resources AEO20201 February 2020 Levelized Cost and Levelized Avoided Cost of New Generation Resources in the Annual Energy Outlook* 2020, https://www.eia.gov/outlooks/aeo/pdf/electricity_generation.pdf, (accessed 7/16/20, 2020).

4 *ERCOT - Grid Information - Generation*, http://www.ercot.com/gridinfo/generation, (accessed 7/16/20, 2020).

5 M. Ulaganathan, V. Aravindan, Q. Yan, S. Madhavi, M. Skyllas-Kazacos and T. M. Lim, *Adv. Mater. Interfaces*, 2016, **3**, 1500309.

6 B. Dunn, H. Kamath and J.-M. Tarascon, *Science*, 2011, **334**, 928–935.

7 C. Zhang, L. Zhang, Y. Ding, S. Peng, X. Guo, Y. Zhao, G. He and G. Yu, *Energy Storage Mater.*, 2018, **15**, 324–350.

8 K. Gong, Q. Fang, S. Gu, S. F. Y. Li and Y. Yan, *Energy Environ. Sci.*, 2015, **8**, 3515–3530.

9 R. W. Hogue and K. E. Toghill, *Curr. Opin. Electrochem.*, 2019, **18**, 37–45.

10 Y. Yan, S. G. Robinson, M. S. Sigman and M. S. Sanford, *J. Am. Chem. Soc.*, 2019, **141**, 15301–15306.

11 N. H. Attanayake, J. A. Kowalski, K. V. Greco, M. D. Casselman, J. D. Milshtein, S. J. Chapman, S. R. Parkin, F. R. Brushett and S. A. Odom, *Chem. Mater.*, 2019, **31**, 4353–4363.

12 K. H. Hendriks, S. G. Robinson, M. N. Braten, C. S. Sevov, B. A. Helms, M. S. Sigman, S. D. Minteer and M. S. Sanford, *ACS Cent. Sci.*, 2018, **4**, 189–196.

13 J. Friedl, M. A. Lebedeva, K. Porfyrakis, U. Stimming and T. W. Chamberlain, *J. Am. Chem. Soc.*, 2018, **140**, 401–405.

14 J. Winsberg, T. Hagemann, T. Janoschka, M. D. Hager and U. S. Schubert, *Angew. Chem., Int. Ed.*, 2017, **56**, 686–711.

15 P. Leung, A. A. Shah, L. Sanz, C. Flox, J. R. Morante, Q. Xu, M. R. Mohamed, C. Ponce de León and F. C. Walsh, *J. Power Sources*, 2017, **360**, 243–283.

16 J. A. Kowalski, M. D. Casselman, A. P. Kaur, J. D. Milshtein, C. F. Elliott, S. Modekrutti, N. H. Attanayake, N. Zhang, S. R. Parkin, C. Risko, F. R. Brushett and S. A. Odom, *J. Mater. Chem. A*, 2017, **5**, 24371–24379.

17 J. D. Milshtein, J. L. Barton, R. M. Darling and F. R. Brushett, *J. Power Sources*, 2016, **327**, 151–159.

18 T. B. Liu, X. L. Wei, Z. M. Nie, V. Sprenkle and W. Wang, *Adv. Energy Mater.*, 2016, **6**, 1501449.

19 G.-M. Weng, B. Yang, C.-Y. Liu, G.-Y. Du, E. Y. Li and Y.-C. Lu, *Energy Environ. Sci.*, 2019, **12**, 2244–2252.

20 J. D. Milshtein, A. P. Kaur, M. D. Casselman, J. A. Kowalski, S. Modekrutti, P. L. Zhang, N. Harsha Attanayake, C. F. Elliott, S. R. Parkin, C. Risko, F. R. Brushett and S. A. Odom, *Energy Environ. Sci.*, 2016, **9**, 3531–3543.

21 Y. Yan, T. P. Vaid and M. S. Sanford, *J. Am. Chem. Soc.*, 2020, **142**, 17564–17571.

22 L. E. VanGelder, B. E. Petel, O. Nachtigall, G. Martinez, W. W. Brennessel and E. M. Matson, *ChemSusChem*, 2018, **11**, 4139–4149.

23 J. M. Stauber, S. Zhang, N. Gvozdik, Y. Jiang, L. Avena, K. J. Stevenson and C. C. Cummins, *J. Am. Chem. Soc.*, 2018, **140**, 538–541.

24 J. Friedl, M. V. Holland-Cunz, F. Cording, F. L. Pfanschilling, C. Wills, W. McFarlane, B. Schricker, R. Fleck, H. Wolfschmidt and U. Stimming, *Energy Environ. Sci.*, 2018, **11**, 3010–3018.

25 P. B. Tsitovich, A. M. Kosswattaarachchi, M. R. Crawley, T. Y. Tittiris, T. R. Cook and J. R. Morrow, *Chemistry*, 2017, **23**, 15327–15331.

26 Y. Li, J. Sniekers, J. Malaquias, X. Li, S. Schaltin, L. Stappers, K. Binnemans, J. Fransaer and I. F. J. Vankelecom, *Electrochim. Acta*, 2017, **236**, 116–121.

27 Y. Ding, Y. Zhao, Y. T. Li, J. B. Goodenough and G. H. Yu, *Energy Environ. Sci.*, 2017, **10**, 491–497.

28 P. J. Cappillino, H. D. Pratt, N. S. Hudak, N. C. Tomson, T. M. Anderson and M. R. Anstey, *Adv. Energy Mater.*, 2014, **4**, 1300566.

29 J. A. Suttil, J. F. Kucharyson, I. L. Escalante-Garcia, P. J. Cabrera, B. R. James, R. F. Savinell, M. S. Sanford and L. T. Thompson, *J. Mater. Chem. A*, 2015, **3**, 7929–7938.

30 Y. Y. Lai, X. Li and Y. Zhu, *ACS Appl. Polym. Mater.*, 2020, **2**, 113–128.

31 E. C. Montoto, G. Nagarjuna, J. S. Moore and J. Rodríguez-López, *J. Electrochem. Soc.*, 2017, **164**, A1688–A1694.

32 R. M. Darling, K. G. Gallagher, J. A. Kowalski, S. Ha and F. R. Brushett, *Energy Environ. Sci.*, 2014, **7**, 3459–3477.

33 H. Huang, R. Howland, E. Agar, M. Nourani, J. A. Golen and P. J. Cappillino, *J. Mater. Chem. A*, 2017, **5**, 11586–11591.

34 T. C. Gokoglan, S. K. Pahari, A. Hamel, R. Howland, P. J. Cappillino and E. Agar, *J. Electrochem. Soc.*, 2019, **166**, A1745–A1751.

35 J. F. Kucharyson, L. Cheng, S. O. Tung, L. A. Curtiss and L. T. Thompson, *J. Mater. Chem. A*, 2017, **5**, 13700–13709.

36 L. Cheng, P. Redfern, K. C. Lau, R. S. Assary, B. Narayanan and L. A. Curtiss, *J. Electrochem. Soc.*, 2017, **164**, E3696–E3701.

37 R. E. Skyner, J. L. McDonagh, C. R. Groom, T. van Mourik and J. B. O. Mitchell, *Phys. Chem. Chem. Phys.*, 2015, **17**, 6174–6191.

38 S.-J. Lu, H.-H. Yang, W.-J. Chang, H.-H. Hsueh, Y.-C. Lin, F.-C. Liu, I. J. B. Lin and G.-H. Lee, *J. Organomet. Chem.*, 2020, **927**, 121543.

39 F. E. Hahn, M. C. Jahnke and T. Pape, *Organometallics*, 2007, **26**, 150–154.

40 E. M. Armstrong, D. Collison, N. Ertok and C. D. Garner, *Talanta*, 2000, **53**, 75–87.

41 A. V. Marenich, C. J. Cramer and D. G. Truhlar, *J. Phys. Chem. B*, 2009, **113**, 6378–6396.

42 J. R. Rumble, *CRC Handbook of Chemistry and Physics*, CRC Press, 101st edn, 2020.

43 E. D. Glendening, C. R. Landis and F. Weinhold, *J. Comput. Chem.*, 2013, **34**, 1429–1437.

44 J. Łubkowski and J. Błażejowski, *Thermochim. Acta*, 1990, **157**, 259–277.

45 P. Dokurno, J. Łubkowski and J. Błàejowski, *Thermochim. Acta*, 1990, **165**, 31–48.

46 J. Błażejowski and E. Kowalewska, *Thermochim. Acta*, 1986, **105**, 257–286.

47 I. Krossing and I. Raabe, *Angew. Chem., Int. Ed.*, 2004, **43**, 2066–2090.

48 P. Atkins and J. De Paula, *Physical Chemistry*, W.H. Freeman and Company, New York, 7 edn, 2002.

49 J. A. Kowalski, A. M. Fenton Jr, B. J. Neyhouse and F. R. Brushett, *J. Electrochem. Soc.*, 2020, **167**, 160513.

50 L. Su, M. Ferrandon, J. A. Kowalski, J. T. Vaughey and F. R. Brushett, *J. Electrochem. Soc.*, 2014, **161**, A1905–A1914.

51 A. M. Kosswattaarachchi, L. E. VanGelder, O. Nachtigall, J. P. Hazelnis, W. W. Brennessel, E. M. Matson and T. R. Cook, *J. Electrochem. Soc.*, 2019, **166**, A464–A472.

52 R. W. Hogue, C. G. Armstrong and K. E. Toghill, *ChemSusChem*, 2019, **12**, 4506–4515.

53 Bruker, *APEX3, SAINT, and SADABS*, Bruker AXS Inc., Madison, Wisconsin, USA, 2008.

54 O. V. Dolomanov, L. J. Bourhis, R. J. Gildea, J. A. K. Howard and H. Puschmann, *J. Appl. Crystallogr.*, 2009, **42**, 339–341.

55 G. Anderegg, E. Koch and E. Bayer, *Inorg. Chim. Acta*, 1987, **127**, 183–188.

56 S. Dermeik and Y. Sasson, *J. Org. Chem.*, 1989, **54**, 4827–4829.

57 F. Neese, *Wiley Interdiscip. Rev.: Comput. Mol. Sci.*, 2012, **2**, 73–78.

58 A. D. Becke, *J. Chem. Phys.*, 1993, **98**, 5648–5652.

59 A. D. Becke, *J. Chem. Phys.*, 1992, **97**, 9173–9177.

60 C. Lee, W. Yang and R. G. Parr, *Phys. Rev. B*, 1988, **37**, 785–789.

61 A. D. Becke, *Phys. Rev. A*, 1988, **38**, 3098–3100.

62 S. H. Vosko, L. Wilk and M. Nusair, *Can. J. Phys.*, 1980, **58**, 1200–1211.

63 T. Lu and F. Chen, *J. Comput. Chem.*, 2012, **33**, 580–592.

64 G. A. Andrienko, *Chemcraft - graphical software for visualization of quantum chemistry computations*, https://www.chemcraftprog.com.